TÜBİTAK

Research Article

Development of a supervised classification method to construct 2D mineral maps on backscattered electron images

Mahmut CAMALAN[1,*] , **Mahmut ÇAVUR**[2]
[1]Middle East Technical University, Ankara, Turkey
[2]Management Information Systems, Kadir Has University, İstanbul, Turkey

Abstract: The Mineral Liberation Analyzer (MLA) can be used to obtain mineral maps from backscattered electron (BSE) images of particles. This paper proposes an alternative methodology that includes random forest classification, a prospective machine learning algorithm, to develop mineral maps from BSE images. The results show that the overall accuracy and kappa statistic of the proposed method are 97% and 0.94, respectively, proving that random forest classification is accurate. The accuracy indicators also suggest that the proposed method may be applied to classify minerals with similar appearances under BSE imaging. Meanwhile, random forest predicts fewer middling particles with binary and ternary composition, but the MLA predicts more middling particles only with ternary composition. These discrepancies may arise because the MLA, unlike random forest, may also measure the elemental compositions of mineral surfaces below the polished section.

Key words: Random forest, Mineral Liberation Analyzer, backscattered electron images, mineral map, confusion matrix

1. Introduction

Mineral maps are particularly used in process mineralogy to obtain quantitative data regarding the morphology and composition of any particle population. These maps can be used to estimate various features of the population such as modal mineralogy [1–4], particle and grain size distributions [5], mineral grade distributions [5–9], mineral associations in binary- and ternary-composed particles [2, 10–14], and grade-recovery curves [2, 11, 12, 15–17].

A mineral map for any sample of particles can be constructed from surface (2D) images of particles. 2D images can be digitized on polished sections of particles by an ore microscope [18] or backscattered electron (BSE) imaging [19, 20] on a scanning electron microscope (SEM). The optical micrographs can be evaluated with various image processing methods [11, 21–26] for the construction of a 2D mineral map on particles. However, the reflected light imaging in ore microscopy generates indistinguishable images of siliceous nonopaque minerals and epoxy resin as the reflected light spectra of the transparent minerals and epoxy resin are very similar [27]. This brings a great limitation to the exclusion of epoxy resin from mineral maps. Some complex algorithms were proposed to segment the borders between nonopaque minerals and epoxy resin for the discrimination of these objects [23, 28]; however, these algorithms may be too difficult for end-users who are not experienced in image processing.

---

*Correspondence: camalanmahmut@gmail.com

1030

A common method to evaluate BSE images for mineral mapping is the Mineral Liberation Analyzer (MLA), a commercial software package integrated into the SEM and the energy-dispersive X-ray spectrometer (EDX). In order to construct the mineral map, the tool evaluates the X-ray spectra collected by EDX over points or areas on BSE images [10, 19, 29–31]. Apart from MLA, image processing methods can be used for the construction of 2D mineral maps from BSE images. A simple method for mapping is gray thresholding over BSE images [19], which assigns the phases to gray colors located in a predetermined set of gray color intervals. The method can be successful only if BSE imaging produces a significant gray color contrast between the solid phases with different densities. If the background (epoxy resin) is significantly lighter than any mineral phase, thresholding can easily separate the background image from any mineral phase in BSE images. However, thresholding may not separate the mineral phases from each other when the minerals have similar densities. Then sophisticated image processing methods may be required to distinguish minerals of similar density. A convenient method for this purpose might be supervised image classification [26] based on the random forest tree (RFT or random forest), a machine learning (ML) algorithm [32, 33]. This algorithm was found to give better accuracy than many ML algorithms when it classified narrowly localized synthetic data (i.e. data in close proximity) with an increasing number of training features [34]. This observation suggests that the RFT is a prospective ML algorithm to classify BSE images of minerals of similar density, as long as sufficiently large numbers of training images and features are supplied to the RFT. Random forest is also expected to discriminate background (epoxy) from particles in BSE images, which had not been accomplished previously by using the same classification method on microscopic images [26]. As the RFT is embedded in user-friendly software, the users do not have to tackle the details of thresholding or other image processing methods. That is to say, the user should only train the original images that correspond to the area of interest (AOI). The RFT automatically classifies the unknown image through a voting scheme based on a number of textural, boundary, noise, and membrane features [35] learned from the original images.

The present study aims to investigate random forest classification for the accurate retrieval of 2D mineral maps from the BSE images of a chromite ore sample. For the purpose of the present study, the accuracy of the method on BSE images was assessed with the confusion matrix. Furthermore, the features of mineral maps predicted from BSE images were compared with the features of mineral maps predicted from the MLA. Additionally, the classification accuracies of the RFT and other reputable ML algorithms were evaluated on the training data set (Section 2) to compare their likely success in accurate mineral mapping from BSE images.

2. Experimental material and procedure

The experimental sample was a chromite ore sample within the size range of –0.425 + 0.300 mm. The modal mineralogy predicted by the MLA (Table 1) suggests that the sample mainly consists of chromite, forsterite (olivine), serpentine, and some minor minerals. These minor mineral surfaces were not predicted one by one by random forest; they were predicted as a cluster.

Table 1. Modal mineralogy of the sample estimated by MLA.

	Mineral							
	Chromite	Forsterite	Serpentine	Augite*	Diopside*	Ilmenite*	Plagioclase*	Mg-oxide*
Area (%)	70.16	14.22	11.48	0.33	1.85	0.74	1.11	0.11

* Minor minerals

A single polished section was prepared for the acquisition of BSE images and for the MLA analysis. The polished section was prepared in a cold-mounting EpoxyCure2 resin and further ground and polished on a series of diamond and velvet discs using a Buehler PowerPro 4000.

The epoxy (background) and the mineral surfaces were predicted with point-by-point X-ray mapping [19] by FEI-QUANTA SEM adapted with the EDAX Genesis XM4i X-ray microanalysis system. The constructed mineral map of approximately 4000 particles was evaluated by MLA DataView software to extract the equivalent circle diameter of particles and mineral grains (μm) as well as the areal mineral composition in each particle (μm^2).

A straightforward methodology (Figure 1) was developed to classify the BSE images for 2D mineral mapping and to measure the classification accuracy. All steps in Figure 1 were performed in Fiji-ImageJ software except for the performance evaluation of classifiers, the confusion matrix, and map evaluation, which were performed in Weka, QGIS, and Clemex Vision, respectively. For the sake of simplicity, the methodology is briefly called "BSE image analysis" throughout the paper. The whole methodology is explained in detail throughout the remaining part of this section.


Figure 1. The steps in the BSE image analysis.

The BSE images of 1400 particles were acquired at $50\times$ magnification by FEI-QUANTA SEM operated at 20 kV accelerating voltage. To increase the accuracy of the next classification step, BSE images were preprocessed by removing the noise on them while exposing the boundaries between different objects (mineral surfaces and epoxy). This stage was achieved by successive application of the Kuwahara [36] and sharpen [37] filters to the BSE images. Kuwahara, an edge-preserving filter, was applied on 5×5 pixel-window subregions to remove the noise on the BSE images without blurring the boundaries between different image features. This optimum window size was selected by judging the qualitative effects of window size on the success of the Kuwahara filter. Then the sharpening filter was applied to expose the object boundaries more by increasing the color contrast in the images. The filter used the following weighting factors of [–1, –1, 1; –1, 12, –1; –1, –1, –1] to replace each pixel with a weighted average of the 3×3 neighborhood. Figures 2a and 2b demonstrate the preprocessed images after successive application of the Kuwahara and sharpen filters, respectively, to a sample BSE image (Figure 2c).

Prior to classification, the performance of random forest was pair-wise evaluated against some powerful machine learning algorithms (naive-Bayes, support vector machine, k-nearest neighbor, C4.5 decision tree, and logistic regression) to assess the adequacy of random forest for BSE image analysis. These ML algorithms were chosen for comparison because many studies suggest that they can work quite accurately with any type of data different in size and dimension [34, 35, 38–40]. The pair-wise comparisons were made between the accuracy indicators (overall accuracy and kappa statistics) of random forest and each selected algorithm on the training data set chosen from the training images (Figure 3). Each test was conducted using the 'Weka experimenter' tool embedded in the Weka segmentation toolbox. The tool initially performed repeated classifications of the training data set with all ML algorithms, simply by splitting 10 equal-sized subsets of the whole data into new training sets and unknown data sets. This resampling technique, called 10-fold cross-validation, is

favored in data science as it provides acceptable variance, low bias, and low computational cost while evaluating the performance of a predictive model [41]. After classification with ML algorithms, two-tailed t-tests were performed between the mean kappa statistics or overall accuracies of each algorithm and random forest. The null hypothesis of each test was that the selected indicators of the ML algorithm and random forest were equal. The null hypothesis was rejected when the P-value of the test was lower than the significance level of 0.05. However, when the difference between the two tested algorithms was statistically significant, the algorithm with higher overall accuracy and kappa statistic was concluded to perform more accurate classification.
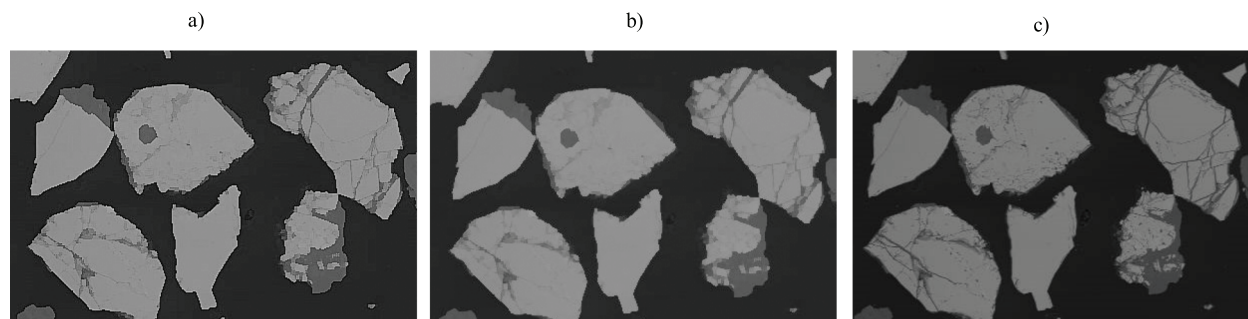

Figure 2. The successive application of the Kuwahara (a) and sharpen (b) filters to a sample image (c).
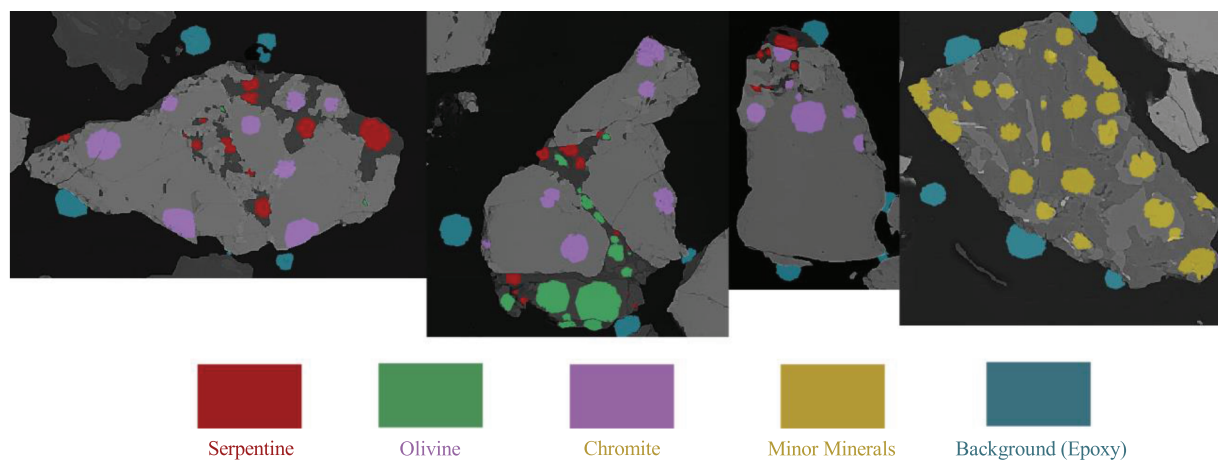

Figure 3. Training feature extraction for the classification of BSE images.

The classification of the preprocessed BSE images was performed with open-source Fiji-ImageJ software [42] using the Trainable Weka Segmentation toolbox [35, 43]. The supervised classification method was the RFT algorithm [32, 33], which predicted five classes (chromite, serpentine, olivine, epoxy, and a cluster of minor minerals) by using random decision trees constructed from the edge detectors, texture filters, noise-reduction filters, and membrane detectors available in the Weka toolbox [43]. The training features were extracted using the blow/lasso tool from four surface images (Figure 3) whose compositions were known to be predicted accurately by the MLA. (Figure 4). Additional care was taken while sampling around the boundaries of different objects to avoid collecting false training data.

Image postprocessing was performed on the classified BSE images to (i) remove residual noise generated by classification and (ii) separate particles erroneously connected by the classification. The removal of residual noise was achieved by applying a 3×3 median filter [44] to the classified BSE images. Then watershed transformation [45] was applied to the classified BSE images (a sample is provided in Figure 5a) to separate particles erroneously connected by the classification (Figure 5b).
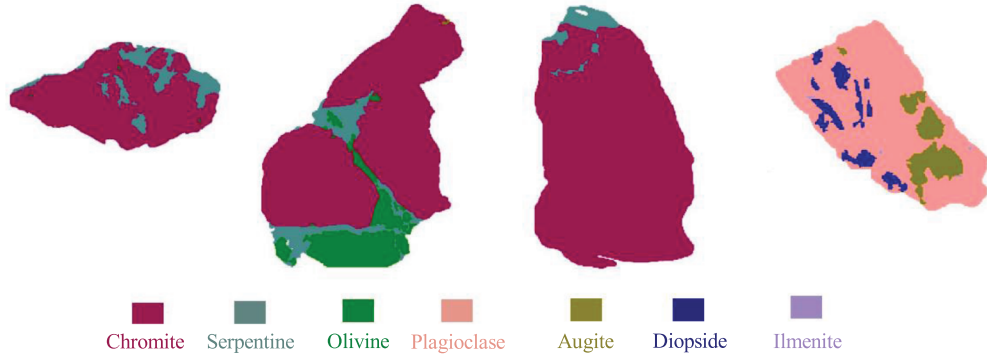
Figure 4. The true mineral compositions of the training samples estimated by the MLA.
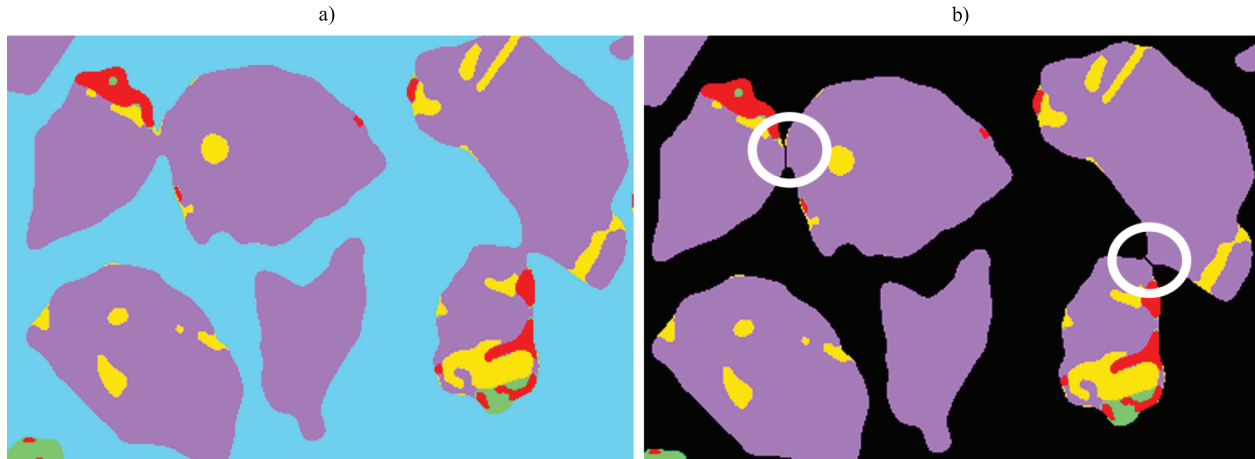

Figure 5. A classified image (a) showing some close particles that were erroneously connected. The final image after watershed transformation (b) in which the connected particles are separated (shown in circles).

The accuracy of the classification method was determined with the confusion matrix [26, 46, 47]. The confusion matrix included a comparison between the true and predicted compositions of a total of 1000 random points on the training images (Figure 3). The random points on the training samples were generated by using QGIS software. The true surface compositions were taken from the mineral maps of some specific training samples (Figure 3) that were correctly predicted by the MLA (Figure 4). The user can use the confusion matrix to describe various indicators that will reflect the success of the classifier and training feature selection. The producer accuracy for any class demonstrates the percentage of correctly classified points of that class on the original image, showing the success of the classifier. The user accuracy for any class is the percentage of true points of that class on the classified image, showing the success of user-dependent training feature selection.

The overall classification accuracy, on the other hand, is the percentage of all points correctly predicted by classification. Meanwhile, the kappa statistic (kappa coefficient) is another indicator to rate the overall accuracy of the classification [48]. A kappa coefficient of one shows perfect agreement between classifier prediction and true class values on the image; however, a coefficient of zero means that the agreement is no better than what would be expected by chance.

The mineral content (μm^2) and the equivalent circle diameters (μm) of particles and grains were calculated from the 2D mineral maps by successively using gray thresholding and Boolean operators in Clemex Vision software. Any particle that touched the image edges was not evaluated at this stage.

The methods described in Sections 3.1–3.4, except watershed transform, were embedded into JavaScript that can be executed over multiple images by using the batch-processing plug-in of ImageJ (Figure 6). The plug-in allowed the automation of most of the image preprocessing, classification, and postprocessing methods on different images. For the batch processing of the classification stage, the plug-in called the classifier file (.model) and the training data (.arff), which had been saved through the Weka Toolbox (Section 3.3), were used. The run time of the whole JavaScript took nearly 2.5 min for each BSE image frame in 1024×884 pixels with a scale of 5.88 μm/pixel. These values suggest that the method classifies 0.26 mm^2 of the polished section in one second, being sufficiently fast for mineral mapping.
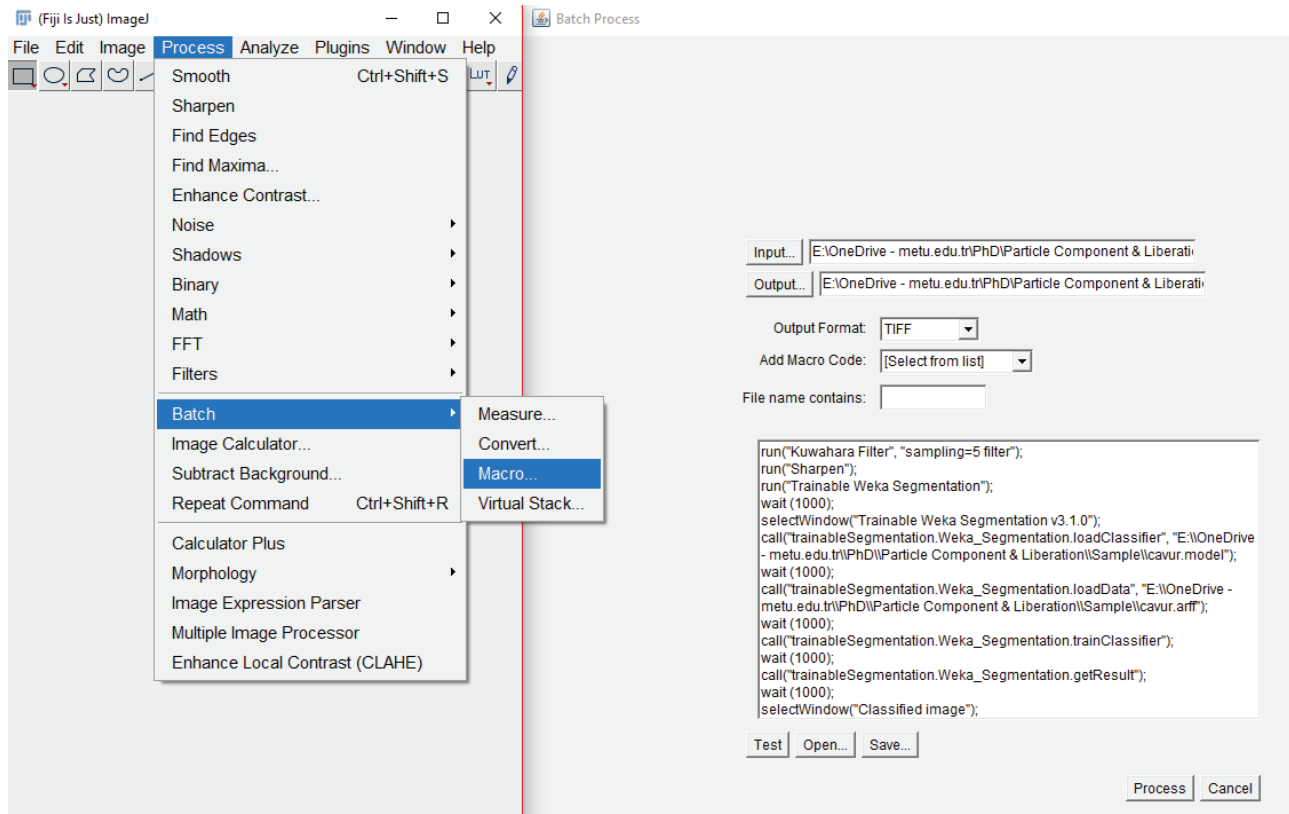
Figure 6. Batch processing plug-in used for the semiautomation of the 2D mapping method.

3. Results and discussion

In Table 2, the average accuracy indicators are given for the random forest, C4.5 decision tree, logistic regression, naive Bayes, k-nearest neighbor, and support vector machine algorithms after 10-fold cross-validation tests on the training data set. The table shows that the average accuracy of random forest classification is significantly the highest among the accuracies of all tested algorithms. Therefore, random forest can be assessed as the most prospective ML algorithm for BSE image analysis. Nevertheless, the other machine learning algorithms have accuracies greater than 90%, indicating that they may also be used for mineral mapping on BSE images. However, the space of the paper is currently limited for developing mineral mapping methodologies that include other ML algorithms coupled with image pre- and postprocessing techniques.

Table 2. The kappa statistics of the random forest, naive Bayes, SVM, and kNN algorithms on the training data set after 10-fold cross-validation performance tests.

Name	Code name in Weka experimenter tool	Overall accuracy	Kappa statistics
Random forest	weka.classifiers.trees.RandomForest	99.98	1
C4.5 decision tree	weka.classifiers.trees.J48	99.91*	0.99*
k-nearest neighbor	weka.classifiers.lazy.IBk	99.88*	0.99*
Logistic	weka.classifiers.functions.Logistic	99.61*	0.99*
Support vector machine	weka.classifiers.functions.SMO	99.55*	0.99*
Naive Bayes	weka.classifiers.bayes.NaiveBayes	91.89*	0.89*

* The difference between the accuracy indicators of the selected algorithm and the random forest tree is statistically significant.

Figure 7 demonstrates a resultant classified image after the BSE image analysis on an unclassified image of a sample of chromite ore particles, which verifies the correctness of the analysis qualitatively. The confusion matrix in Table 3 shows that all the accuracy indicators including the producer and user accuracies for the objects are quite high as well as the overall accuracy and kappa statistics (Section 3.5), proving that the classifier works accurately for all the minerals and epoxy. The high accuracy for the background (epoxy) classification will indicate a high success on the background extraction that cannot be accomplished on ore-microscopy images [26]. Table 3 also shows that the producer accuracy of olivine is slightly lower than the accuracies of other minerals, because of the misclassification of olivine as serpentine. These silicate minerals have similar densities; therefore, they yield similar gray colors under BSE imaging, which may reduce the success of their discrimination by random forest. The MLA might also face an analogous problem because these minerals have similar compositions; therefore, they cannot be distinguished by their EDX spectra such as hematite and magnetite [49]. Nevertheless, the producer accuracies of all minerals are quite high in the BSE image analysis (Table 3), suggesting that random forest may be sufficient to differentiate minerals with similar appearances.

Figures 8a and 8b show the modal mineralogy and particle size distributions, respectively, which were predicted by BSE image analysis and the MLA. These figures show that both analyses predict a similar modal mineralogy and particle size distribution. Then one can initially think both analyses should produce the same mineral map. However, there were some indicators opposing this assumption. As demonstrated in Figure 9a, the grade distributions predicted from BSE images and MLA analysis are very similar except at the distribution of chromite-rich particles: random forest predicts that chromite-rich particles are distributed in the fully liberated chromite grains (particles having chromite grade of 100 %), but the MLA assigns chromite-rich particles to the apparently liberated chromite grains (particles having chromite grade between 80% and 99.9%). As a result,

Unclassified Image   Classified Image
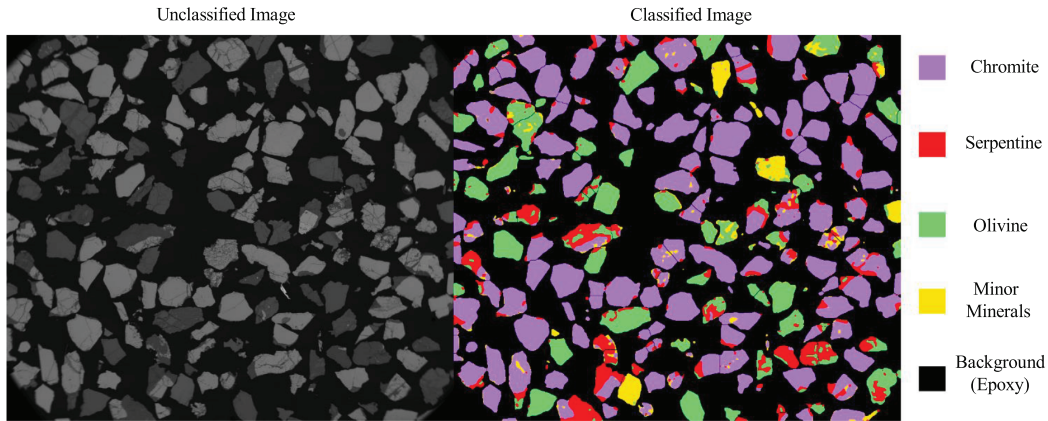
Figure 7. The classified and unclassified image of a sample of chromite ore particles.

Table 3. Confusion matrix for the image classification.

		Predicted class						
		Background	Chromite	Serpentine	Olivine	Minor minerals	Total	Producer accuracy (%)
True class	Background	406	0	0	1	2	409	99.27
	Chromite	1	362	4	0	1	368	98.37
	Serpentine	1	0	62	0	0	63	98.41
	Olivine	0	0	3	26	0	29	89.66
	Minor minerals	2	0	5	2	122	131	93.13
	Total	410	362	74	29	125	1000	
	User accuracy (%)	99.02	100	83.78	89.66	97.60		
Overall accuracy (%)								97.80
Kappa statistics								0.94

BSE image analysis predicts a grade-recovery plot shifting higher from the plot predicted by the MLA, i.e. the former analysis overestimates the surface of liberated chromite grains with respect to the latter (Figure 9b). Meanwhile, Table 4 gives the percent distribution of chromite surfaces to the free (liberated), binary, and ternary particles, which is predicted by the BSE image analysis and the MLA. The table shows that the MLA distributes all chromite grains to the ternary particles, whereas the BSE image analysis distributes chromite to both binary and ternary particles. Figure 10 demonstrates the number-weighted grain size distributions of chromite, serpentine, and olivine minerals estimated with the MLA and the BSE image analysis. The figure shows that only the grain-size distributions of chromite predicted by the two methods (Figure 10a) overlap with the particle size distributions of the ore sample predicted by the methods (Figure 8b). This shows that particles are mostly chromite grains and the other minerals might be locked with chromite. Meanwhile, the MLA predicts the grain size distributions of serpentine (Figure 10b) and olivine (Figure 10c) finer than the BSE image analysis does. The finer silicate grains are likely to lock with chromite grains and form ternary particles rather than free or binary particles, which is consistent with the chromite association behavior predicted by the MLA (Table 4).
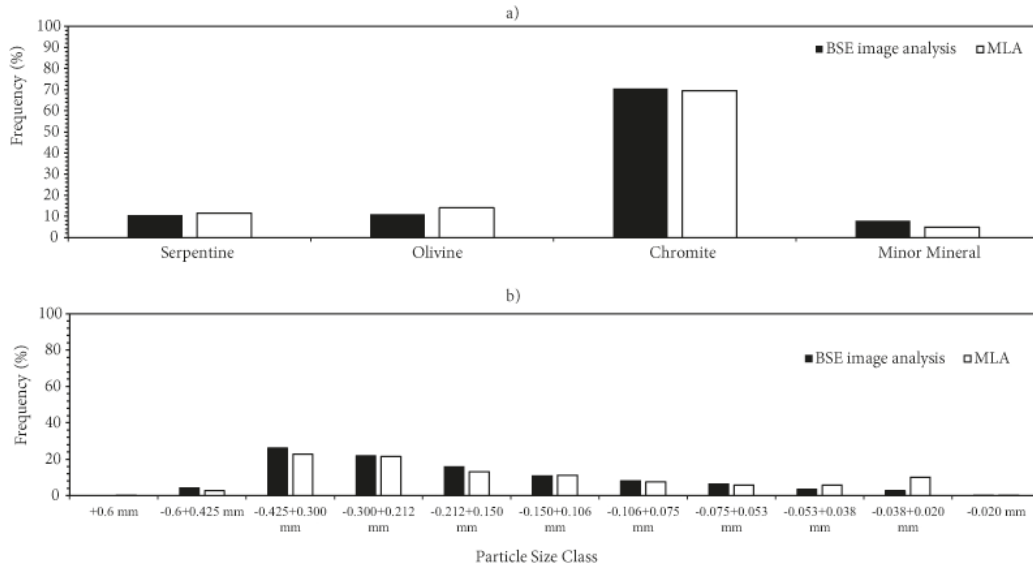
Figure 8. The number-based particle size distributions estimated with the BSE image analysis and MLA.
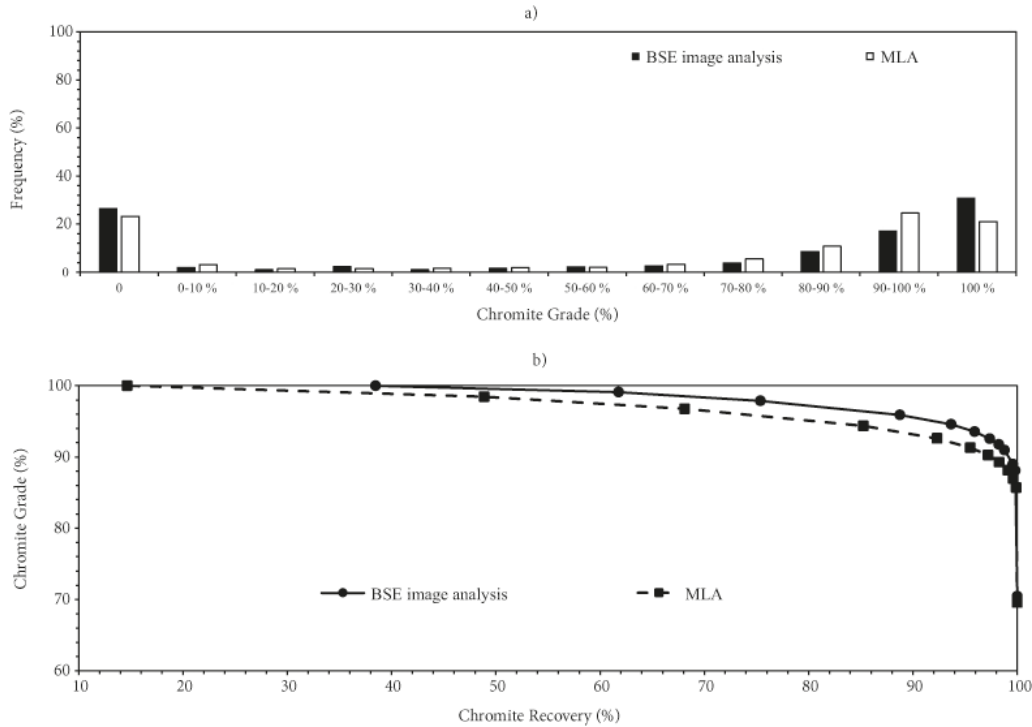
Figure 9. The chromite grade distributions (a) and chromite grade recovery curves (b) estimated with BSE image analysis and microscopic analysis.

The abovementioned discrepancies between the mineral maps of the MLA and BSE image analysis may be associated with some uncertainties in MLA measurement since the accuracy indicators in random forest are quite high. We suspect that one significant uncertainty may arise from the high interaction volume of the X-ray
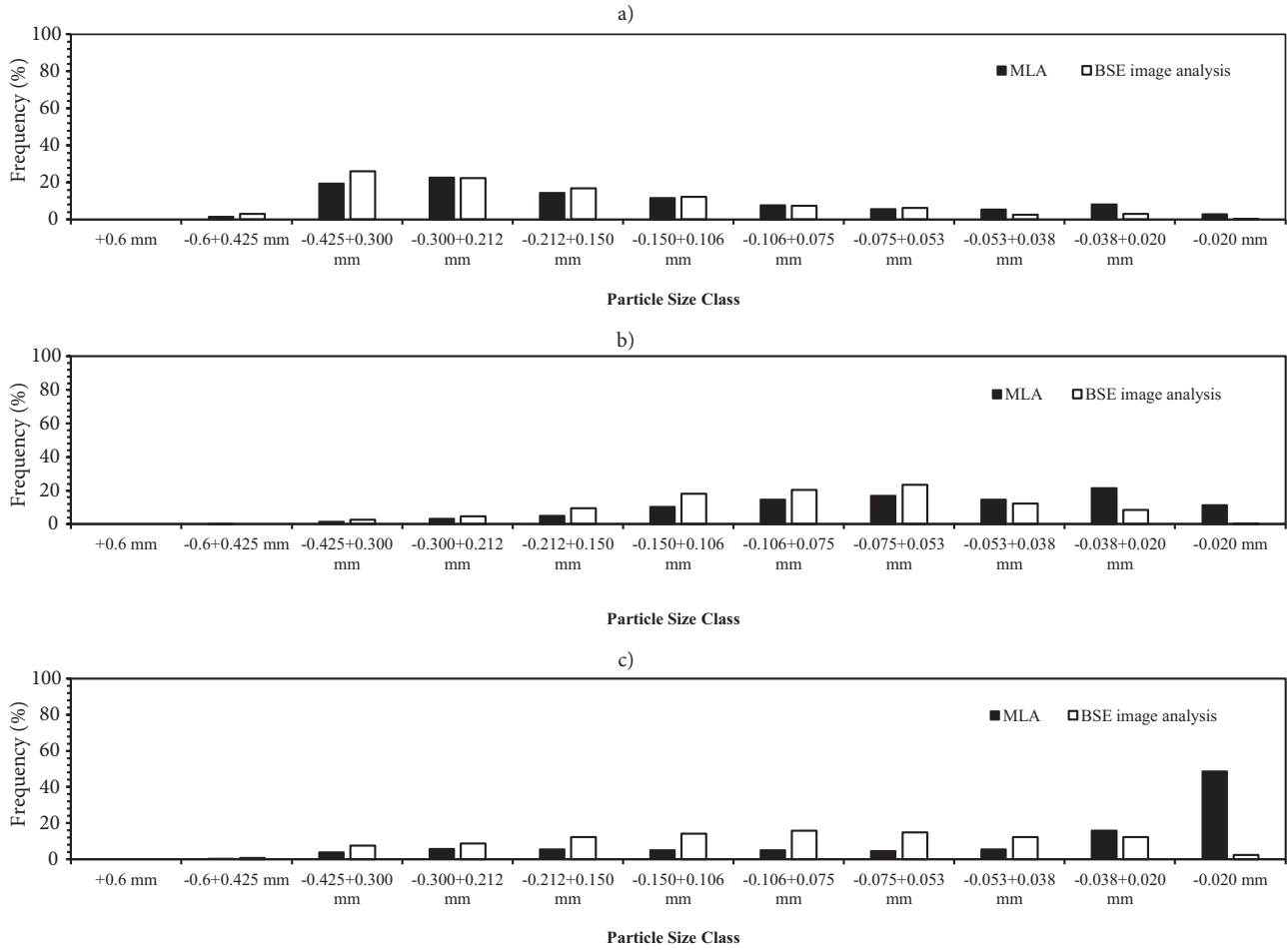
Figure 10. The number-based grain size distributions of chromite (a), serpentine (b), and olivine (c) predicted by the BSE image analysis and MLA.

Table 4. Distribution of chromite to free, binary, and ternary particles predicted with the BSE image analysis and MLA.

BSE image analysis	Free particles	Binary particles		Ternary particles
Percentage of chromite mineral surface distributed to	38.49	Serpentine	Olivine	41.14
		20.38	0.00	
MLA	Free particles	Binary particles		Ternary particles
Percentage of chromite mineral surface distributed to	14.67	Serpentine	Olivine	82.91
		0.00	2.42	

spectra during MLA measurement. The interaction volume, accordingly, can be defined as the space in which the electron and X-ray scattering events will occur when the incident scanning electrons interact with the solid sample [50]. Even though the backscattered electrons are collected from the polished section surfaces, the X-ray spectra of mineral grains may also be emitted below the polished section as the interaction volume of X-ray scattering is higher than the volume of backscattered electron scattering [51]. If these spectra are collected by

EDX detectors and further evaluated by the MLA software, the measured composition will not correspond to the exact mineral composition of the polished surface but to the average mineral composition of some depth below the polished surface.

4. Conclusions and recommendations

The supervised image classification method can be used to construct an accurate mineral map from BSE images of chromite ore particles. Furthermore, the high accuracy (97.8%) and high kappa statistics (0.94) of random forest classification prove that the method is indeed successful at mapping adherent mineral grains in particles as well as separating the background (epoxy) from particles. The 10-fold cross-validation tests also suggest that random forest will be significantly the most accurate machine learning algorithm for mineral mapping from BSE images. Nevertheless, the accuracy of the other machine learning algorithms is still high, suggesting that they may be coupled with image pre- and postprocessing techniques for mineral mapping.

The method is semiautomated and significantly fast for 2D mineral mapping. Even though most of the method steps are straightforward techniques in image processing, the simplicity of the algorithm coupled with the high classification accuracy proves the uniqueness of the method for 2D mineral mapping.

The results prove the success of the method to classify serpentine and olivine minerals, which have similar appearances on BSE images. Thus, the method may be used to classify other minerals that are difficult to differentiate under BSE, such as hematite and magnetite or chalcopyrite and pyrite. Future studies are required to test the applicability of the methodology for mineral mapping of other ore samples.

The acquired map yields the same modal mineralogy and particle size distribution as the one generated by the MLA. However, the supervised classification will predict fewer middling particles with binary and ternary composition, whereas the MLA predicts more middling particles only with ternary composition. We suspect that this discrepancy may arise because the MLA may inevitably measure the compositions of minerals beneath the polished surface.

References

[1] Charikinya E, Bradshaw S, Becker M. Characterizing and quantifying microwave induced damage in coarse sphalerite ore particles. Minerals Engineering 2015; 82: 14-24. doi: 10.1016/j.mineng.2015.07.020

[2] Sandmann D, Gutzmer J. Use of Mineral Liberation Analysis (MLA) in the characterization of lithium-bearing micas. Journal of Minerals and Materials Characterization and Engineering 2013; 1: 285-292.

[3] Batchelor AR, Jones DA, Plint S, Kingman SW. Increasing the grind size for effective liberation and flotation of a porphyry copper ore by microwave treatment. Minerals Engineering 2016; 94: 61-75. doi: 10.1016/j.mineng.2016.05.011

[4] Pascoe RD, Power MR, Simpson B. QEMSCAN analysis as a tool for improved understanding of gravity separator performance. Minerals Engineering 2007; 20: 487-495. doi:10.1016/j.mineng.2006.12.012

[5] Little L, Mainza AN, Becker M, Wiese JG. Using mineralogical and particle shape analysis to investigate enhanced mineral liberation through phase boundary fracture. Powder Technology 2016; 301: 794-804. doi: 10.1016/j.powtec.2016.06.052

[6] Bérubé MA, Marchand JC. Evolution of the mineral liberation characteristics of an iron ore undergoing grinding. International Journal of Mineral Processing 1984; 13: 223-237. doi: 10.1016/0301-7516(84)90005-X

[7] King RP. Particle populations and distribution functions. In: King RP (editor). Modeling and Simulation of Mineral Processing Systems. Oxford, UK: Butterworth-Heinemann, 2001, pp. 5-43.

[8] Lyman GJ. Method for interpolation of 2-D histogram data: application to mineral liberation data. Powder Technology 1995; 83: 133-138. doi: 10.1016/0032-5910(94)02949-O

[9] Schneider CL. Measurement and calculation of liberation in continuous milling circuit. PhD, University of Utah, Salt Lake City, UT, USA, 1995.

[10] Petruk W. Applied Mineralogy in the Mining Industry. Ottawa, Canada: Elsevier, 2000.

[11] Lane GR, Martin C, Pirard E. Techniques and applications for predictive metallurgy and ore characterization using optical image analysis. Minerals Engineering 2008; 21: 568-577. doi: 10.1016/j.mineng.2007.11.009

[12] Zhong C, Xu C, Lyu R, Zhang Z, Wu X et al. Enhancing mineral liberation of a Canadian rare earth ore with microwave pretreatment. Journal of Rare Earths 2018; 36: 215-224. doi: 10.1016/j.jre.2017.08.007

[13] Quinteros J, Wightman E, Johnson NW, Bradshaw D. Evaluation of the response of valuable and gangue minerals on a recovery, size and liberation basis for a low-grade silver ore. Minerals Engineering 2015; 74: 150-155. doi: 10.1016/j.mineng.2014.12.019

[14] Devasahayam S. Predicting the liberation of sulfide minerals using the breakage distribution function. Mineral Processing and Extractive Metallurgy Review 2014; 36: 136-144. doi: 10.1080/08827508.2014.898638

[15] Medina JF. Liberation-limited grade/recovery curves for auriferous pyrite ores as determined by high resolution x-ray microtomography. PhD, University of Utah, Salt Lake City, UT, USA, 2012.

[16] Finch JA, Gomez CO. Separability curves from image analysis data. Minerals Engineering 1989; 2: 565-568. doi: 10.1016/0892-6875(89)90090-3

[17] Leißner T, Mütze T, Bachmann K, Rode S, Gutzmer J et al. Evaluation of mineral processing by assessment of liberation and upgrading. Minerals Engineering 2013; 53: 171-173. doi: 10.1016/j.mineng.2013.07.018

[18] Craig JR, Vaughan DJ. Ore Microscopy and Ore Petrography. New York, NY, USA: John Wiley & Sons, 1994.

[19] Fandrich R, Gu Y, Burrows D, Moeller K. Modern SEM-based mineral liberation analysis. International Journal of Mineral Processing 2007; 84: 310-320. doi: 10.1016/j.minpro.2006.07.018

[20] Zhou J, Gu Y. Geometallurgical characterization and automated mineralogy of gold ores. In: Adams MD (editor). Gold Ore Processing. Amsterdam, Netherlands: Elsevier, 2016, pp. 95-111.

[21] Celik IB, Can NM, Sherazadishvili J. Influence of process mineralogy on improving metallurgical performance of a flotation plant. Mineral Processing and Extractive Metallurgy Review 2010; 32: 30-46. doi: 10.1080/08827508.2010.509678

[22] Donskoi E, Suthers SP, Fradd SB, Young JM, Campbell JJ et al. Utilization of optical image analysis and automatic texture classification for iron ore particle characterisation. Minerals Engineering 2007; 20: 461-471. doi: 10.1016/j.mineng.2006.12.005

[23] Delbem ID, Galéry R, Brandão PRG, Peres AEC. Semi-automated iron ore characterisation based on optical microscope analysis: quartz/resin classification. Minerals Engineering 2015; 82: 2-13. doi: 10.1016/j.mineng.2015.07.021

[24] Köse C, Alp İ, İkibaş C. Statistical methods for segmentation and quantification of minerals in ore microscopy. Minerals Engineering 2012; 30: 19-32. doi: 10.1016/j.mineng.2012.01.008

[25] Hunt J, Berry R, Walters S. Using mineral maps to rank potential processing behaviour. In: 25th International Mineral Processing Conference, Brisbane, Australia; 2010. pp. 2899-2905.

[26] Camalan, Çavur M, Hoşten Ç. Assessment of chromite liberation spectrum on microscopic images by means of a supervised image classification. Powder Technology 2017; 322: 214-225. doi: 10.1016/j.powtec.2017.08.063

[27] Neumann R, Stanley CJ. Specular reflectance data for quartz and some epoxy resins: implications for digital image analysis based on reflected light optical microscopy. In: Proceedings of the 9th International Congress for Applied Mineralogy. Brisbane, Australia; 2008. pp. 703-706.

[28] Poliakov A, Donskoi E. Automated relief-based discrimination of non-opaque minerals in optical image analysis. Minerals Engineering 2014; 55: 111-124. doi: 10.1016/j.mineng.2013.09.014

[29] Gu Y. Automated scanning electron microscope based mineral liberation analysis. Journal of Minerals & Materials Characterization & Engineering 2003; 2: 33-41.

[30] Sylvester PJ. Use of the mineral liberation analyzer (MLA) for mineralogical studies of sediments and sedimentary rocks. In: Quantitative Mineralogy and Microanalysis of Sediments and Sedimentary Rocks. St. John's, NL, Canada: Mineralogical Association of Canada Short Course Series 42, 2012, pp. 1-16.

[31] Vizcarra TG, Wightman EM, Johnson NW, Manlapig EV. The effect of breakage mechanism on the mineral liberation properties of sulphide ores. Minerals Engineering 2010; 23: 374-382. doi: 10.1016/j.mineng.2009.11.012

[32] Breiman L. Random forests. Machine Learning 2001; 45: 5-32. doi: 10.1023/A:1010933404324

[33] Huang JJ, Siu WC, Liu TR. Fast image interpolation via random forests. IEEE Transactions on Image Processing 2015; 24: 3232-3245. doi: 10.1109/TIP.2015.2440751

[34] Amancio DR, Comin CH, Casanova D, Travieso G, Bruno M et al. A systematic comparison of supervised classifiers. PLoS ONE 2014; 9: 1-14. doi: 10.1371/journal.pone.0094137

[35] Arganda-Carreras I, Kaynig V, Schindelin J, Cardona A, Seung HS. Trainable Weka segmentation: a machine learning tool for microscopy image segmentation. In: Neuroscience 2014 Short Course 2 - Advances in Brain-scale, Automated Anatomical Techniques: Neuronal Reconstruction, Tract Tracing, and Atlasing. 2014, pp. 73-80.

[36] Bartyzel K. Adaptive Kuwahara filter. Signal, Image and Video Processing 2016; 10: 663-670. doi: 10.1007/s11760-015-0791-3

[37] Praveen KS, Babu KP, Sreenivasulu M. Implementation of image sharpening and smoothing using filters. International Journal of Scientific Engineering and Applied Science 2016; 2: 7-14.

[38] Shavlik JW, Mooney RJ, Towell GG. Symbolic and neural learning algorithms: an experimental comparison. Machine Learning 1991; 6: 111-143.

[39] Meyer D, Leisch F, Hornik K. The support vector machine under test. Neurocomputing 2003; 55: 169-186.

[40] Huang J, Ling CX. Using AUC and accuracy in evaluating learning algorithms. IEEE Transactions on Knowledge and Data Engineering 2005; 17: 299-310.

[41] Kuhn M, Johnson, K. Applied Predictive Modeling. New York, NY, USA: Springer, 2013.

[42] Lind R. Open source software for image processing and analysis: picture this with ImageJ. In: Harland L, Forster M (editors). Open Source Software in Life Science Research, Woodhead Publishing Limited, 2012: pp. 131-149.

[43] Arganda-Carreras I, Kaynig V, Rueden C, Eliceiri KW, Schindelin J et al. Trainable Weka segmentation: a machine learning tool for microscopy pixel classification. Bioinformatics 2017; 33: 2424-2426. doi: 10.1093/bioinformatics/btx180

[44] Khorram F, Memarian H, Tokhmechi B. Limestone chemical components estimation using image processing and pattern recognition techniques. Journal of Mining & Environment 2011; 2: 126-135.

[45] Soille P, Vincent LM. Determining watersheds in digital pictures via flooding simulations. In: Kunt M (editor). SPIE Visual Communications and Image Processing '90, 1990: pp. 240-250.

[46] Fawcett T. An introduction to ROC analysis. Pattern Recognition Letters 2006; 27: 861-874.

[47] Stehman SV. Selecting and interpreting measures of thematic classification accuracy. Remote Sensing of Environment 1997; 62: 77-89. doi: 10.1016/S0034-4257(97)00083-7

[48] Murty PS, Tiwari H. Accuracy assessment of land use classification — a case study of Ken Basin. Journal of Civil Engineering and Architecture Research 2015; 2: 1199-1206.

[49] Figueroa G, Moeller K, Buhot M, Gloy G, Haberlah D. Advanced discrimination of hematite and magnetite by automated mineralogy. In: Proceedings of the 10th International Congress for Applied Mineralogy (ICAM); Berlin, Germany; 2011. pp. 197-204.

[50] Goldstein JI, Newbury DE, Michael JR, Ritchie NWM, Scott JHJ et al. Scanning Electron Microscopy and X-ray Microanalysis. New York, NY, USA: Springer, 2018.

[51] Reichelt R. Scanning Electron Microscopy. In: Hawkes PW, Spence JCH (editors). Science of Microscopy. New York, NY, USA: Springer, 1997, pp. 133-272.